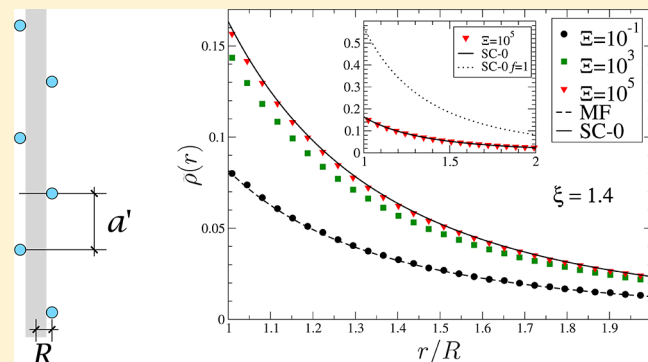


Counterion Density Profile around Charged Cylinders: The Strong-Coupling Needle Limit

Juan Pablo Mallarino,^{*,†} Gabriel Téllez,^{*,†} and Emmanuel Trizac^{*,‡}[†]Departamento de Física, Universidad de los Andes - Bogotá, Colombia[‡]Laboratoire de Physique Théorique et Modèles Statistiques (UMR CNRS 8626), Université Paris-Sud, F-91405 Orsay, France**S** Supporting Information

ABSTRACT: Charged rod-like polymers are not able to bind all their neutralizing counterions: a fraction of them evaporates, while the others are said to be condensed. We study here counterion condensation and its ramifications, both numerically by means of Monte Carlo simulations employing a previously introduced powerful logarithmic sampling of radial coordinates and analytically, with special emphasis on the strong-coupling regime. We focus on the thin rod or needle limit that is naturally reached under strong Coulombic couplings, where the typical intercounterion spacing a' along the rod is much larger than its radius R . This regime is complementary and opposite to the simpler thick rod case where $a' \ll R$. We show that due account of counterion evaporation, a universal phenomenon in the sense that it occurs in the same clothing for both weakly and strongly coupled systems, allows one to obtain excellent agreement between the numerical simulations and the strong-coupling calculations.



1. INTRODUCTION

Some linear biopolymers are intrinsically stiff objects, further rigidified by electric charges along their backbone. This is the case of double stranded DNA, tubulin, actin, and some viruses. These macromolecules may be envisioned, to first approximation, as straight charged cylinders, attracting neutralizing counterions through a logarithmic potential. It was first realized by Onsager that this functional form is similar to that of the confinement entropy, so that not all counterions are bound to the polymer:¹ a finite fraction only remains confined in the limit of infinite system size, with no external boundary; above a certain critical temperature, all counterions evaporate.

The phenomenon of counterion condensation/evaporation has been central in a consequential number of studies since the 1970s, for it is cardinal in a wealth of static and dynamic properties of charged polymers;^{1–6} see, e.g., refs 7–11 for more exhaustive references. It is governed by the so-called Manning parameter ξ , which is the dimensionless line charge of the rod: $\xi = ql_B\lambda$, defined from the valency q of counterions, the linear charge λe , and the Bjerrum length $l_B = e^2/(4\pi\epsilon kT)$, where ϵ is the dielectric constant of the medium, e is the elementary charge, and kT denotes thermal energy. Interestingly, the mean field (Poisson–Boltzmann¹²) scenario of a complete evaporation of ions for $\xi < 1$ in an infinite system and of a partial condensation for $\xi > 1$ also holds beyond mean field,^{5,9} when Coulombic couplings are important. Such couplings are conveniently quantified by the parameter $\Xi = q^2 l_B \xi / R$ where R is the cylinder radius. It is defined to match its planar counterpart $\Xi = 2\pi q^3 l_B^2 \sigma$,^{10,13} where σe is the surface charge of the colloid considered, with here $\sigma = \lambda/(2\pi R)$.

While ξ and Ξ both measure the inverse temperature, their scaling with $1/T$ differs and their roles in the forthcoming analysis are somewhat asymmetric. In essence, Ξ governs the distance to mean field, in the sense that the Poisson–Boltzmann theory becomes exact for $\Xi \rightarrow 0$, and remains accurate for small Ξ . In the present work, we will focus on the opposite limit of large Ξ values, which defines the strong-coupling regime for which mean field is invalid. One may naively think that the Manning parameter should also be large for a strong-coupling approach to hold, but we will see that the situation is more subtle, and some quantities can be obtained for arbitrary values of ξ provided Ξ is large. It is important though to clearly discriminate the thin and thick cylinder cases, because they involve different mechanisms. To see this, we start with a cylinder with large radius, where “large” means that R significantly exceeds the typical distance a between ions when they are close to their ground state. The situation is locally that depicted in Figure 1 and is mostly governed by the planar geometry physics studied in refs 13–16 up to some curvature corrections that have not been studied so far. From the electroneutrality requirement $\sigma a^2 \propto q$, we obtain that $\xi \gg \Xi^{1/2}$ for thick rods. For the sake of the discussion, we restrict here on ground state considerations, and will address thermal effects in detail later on. Gradually decreasing R at fixed σ

Special Issue: Peter G. Wolynes Festschrift**Received:** December 3, 2012**Revised:** February 15, 2013**Published:** February 25, 2013

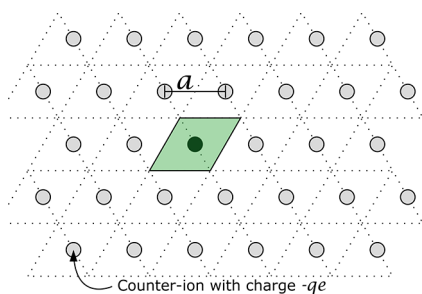


Figure 1. The Wigner crystal formed for $\Xi \rightarrow \infty$ at weakly curved quasi-planar cylinder (thick cylinder case, $a \ll R$). The shaded region is the cell area per counterion at the surface. Up to a numerical prefactor, we have $a \propto (q/\sigma)^{1/2}$. At finite but large Ξ , such an idealized configuration is met for $\xi \gg \Xi^{1/2}$.

(with fixed Ξ and decreasing ξ), one encounters typical configurations such as that depicted in Figure 2 where a and R

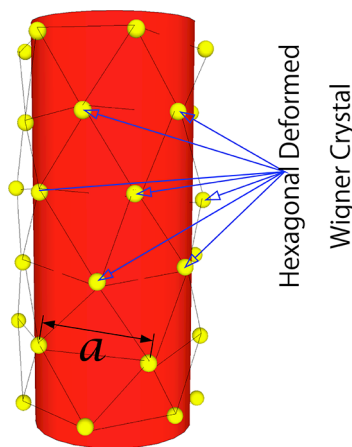


Figure 2. Artist's view of counterions at the charged cylinder for large Ξ , with a and R of like magnitude. Here, ξ is comparable to $\Xi^{1/2}$.

are comparable, before reaching the thin or needle case sketched in Figure 3, where $\xi \ll \sqrt{\Xi}$ ($a \gg R$), and that will be the center of our interest. The reason is that a common and experimentally relevant way to raise Coulombic couplings in a soft matter system is to increase the counterion valency q . Given that $\Xi^{1/2}/\xi \propto (q/(\lambda R))^{1/2}$, we see that this ultimately leads to $\xi \ll \sqrt{\Xi}$. It may be noted that the ground state, reached, e.g., at $T \rightarrow 0$, corresponds to both diverging Ξ and ξ parameters, but the ratio $\Xi^{1/2}/\xi$ is a geometric quantity, independent of the temperature. In the needle limit, the relevant length scale to measure counterion distances is no longer a , defined as a two-dimensional quantity, but its one-dimensional counterpart a' (see Figure 3). We can obtain an order of magnitude assuming all ions are condensed onto the rod, which leads to¹⁷ $a' \simeq q/\lambda$. This is a lower bound, since the phenomenon of counterion evaporation invariably leads to a lower linear charge than λe . We emphasize here that, although previous studies seem to have overlooked the key difference between the thick and thin cylinder cases, the parameter Ξ/ξ^2 has been identified as crucial for the interactions between like-charged rods in ref 18, and also appears in ref 19.

As alluded to above, we consider an infinitely long charged cylinder of radius R , within the primitive cell model (see Figure 4): point counterions with charge $-qe$ are confined in a coaxial larger cylinder of radius D . The ions may equally have a small hard core, which is immaterial here. We thus deal with a salt-free system.

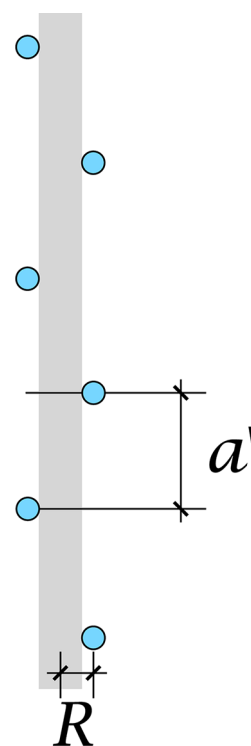


Figure 3. Schematic representation of the ground state in the *needle limit*, that is, for $\xi \ll \sqrt{\Xi}$. The distance between charges is denoted a' , and we have $a' \gg a \gg R$.

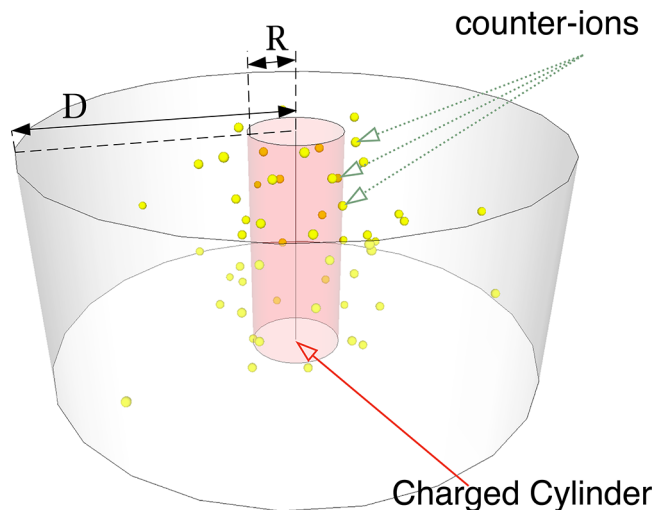


Figure 4. The 3D cylindrical cell model. The rod is assumed positively charged, and the counterions are therefore negative, with charge $-qe$.

The solvent is accounted for through its uniform dielectric constant ϵ . No dielectric discontinuity is considered here between the solvent and the charged cylinder; see, e.g., ref 19 for inclusion of a dielectric mismatch. Charged species interact with three-dimensional Coulomb potential, varying as the inverse distance for point particles, with an additional hard-core term that prevents the ions from entering the charged cylinder.

The outline of the paper is as follows. We first remind you of some relevant and known results pertaining to mean field in section 2 before presenting in section 3 our strong-coupling (SC) analysis. For a given value of Manning parameter ξ , we work out in a first step the leading order behavior of the density

profile when the coupling parameter $\Xi \rightarrow \infty$. The present problem in the needle limit is a case where, in principle and for the leading order only, the virial strong-coupling approach put forward by Netz and collaborators^{5,9,10,14,15,20,21} should coincide with its Wigner-SC counterpart worked out in refs 13 and 16. However, due to a different treatment of counterion evaporation, our leading SC expressions (SC-0) will differ from previously published “virial” results.^{5,9} We will see that these virial results do not account for counterion evaporation, and are consequently improperly normalized. In a second step, we will derive the next correction to SC-0 in the strong-coupling expansion, following the Wigner picture of refs 13 and 16, since it has been shown that the virial approach fails in this task.¹⁶ Section 4 will contain the essentials of the Monte Carlo method used for numerical simulations. Since the evaporation phenomenon exhibits particularly pronounced finite-size effects (a phenomenon that was most clearly identified in refs 5 and 9), we will resort to exponentially large system sizes [with typically $\log(D/R)$ on the order of a few hundreds], adopting the efficient centrifugal sampling scheme devised in ref 9. The comparison between the analytical predictions and simulation data will be provided in sections 5 and 6. Some emphasis will be on density profiles, but an order parameter for the condensation phenomenon and pair correlation properties will also be analyzed (section 5). While most simulations have been performed with system sizes that are large enough and not plagued by finite-size effects, the consequences of decreasing the system size will be addressed in section 6. Finally, section 7 contains our conclusions. The technical content of the presentation has been lightened by delegating details to the complementary sections.

2. MEAN FIELD

We recall in this section some known results from the mean field (Poisson–Boltzmann) theory.^{9,12} The nonlinear Poisson–Boltzmann equation admits an analytic solution often attributed to Katchalski et al.^{22–24} but which seems to date back to Liouville.²⁵ This solution brings to the fore the importance of a large lateral extension parameter [$\Delta = \log(D/R)$, with R and D the charged cylinder radius and the outer cylinder cell radius respectively; see Figure 4]. The Poisson–Boltzmann equation reads, outside the charged cylinder ($r \geq R$),

$$\nabla_{\tilde{r}}^2 u(\tilde{r}) = \tilde{k}_D^2 e^u(\tilde{r}) \quad (1)$$

where $u(\tilde{r}) = -\beta q e \Phi(r)$ is the dimensionless potential and r the radial distance. Tilde distances are made dimensionless with the Gouy–Chapman length $\mu = R/\xi$ ($\tilde{r} = r/\mu$, $\tilde{R} = R/\mu = \xi$), and \tilde{k}_D is a constant that has no significance before a reference value (a gauge) is chosen for the potential. Equation 1 is supplemented with the boundary conditions $\partial_{\tilde{r}} u(\tilde{D}) = 0$ (global neutrality of the cell) and $\tilde{R}(\partial_{\tilde{r}} u(\tilde{R})) = -2\xi$ (from Gauss’ theorem, normal component of the electric field proportional to the surface charge of the cylinder).

The analytic solution depends on the Fuoss critical parameter $\xi_c = \Delta/(1 + \Delta)$. Here,

$$u(\tilde{r}) = \begin{cases} -\log \left[\frac{k_D^2 \tilde{r}^2}{2\alpha^2} \sinh^2 \left(\alpha \log \frac{\tilde{r}}{\tilde{R}} + \coth^{-1} \frac{\xi - 1}{\alpha} \right) \right] & \xi \leq \xi_c \\ -\log \left[\frac{k_D^2 \tilde{r}^2}{2\alpha^2} \sin^2 \left(\alpha \log \frac{\tilde{r}}{\tilde{R}} + \cot^{-1} \frac{\xi - 1}{\alpha} \right) \right] & \xi \geq \xi_c \end{cases} \quad (2)$$

where α is given by the transcendental equations

$$\xi = \begin{cases} \frac{1 - \alpha^2}{1 - \alpha \coth(-\alpha\Delta)} & \text{if } \xi \leq \xi_c \\ \frac{1 + \alpha^2}{1 - \alpha \cot(-\alpha\Delta)} & \text{if } \xi \geq \xi_c \end{cases} \quad (3)$$

The corresponding dimensionless density $\tilde{\rho} = \rho/(2\pi l_B \sigma^2)$ reads

$$\tilde{\rho}(\tilde{r}) = \frac{\alpha^2}{\tilde{r}^2} \times \begin{cases} \sinh^{-2} \left(\alpha \log \frac{\tilde{r}}{\tilde{R}} + \coth^{-1} \frac{\xi - 1}{\alpha} \right) & \xi \leq \xi_c \\ \sinh^{-2} \left(\alpha \log \frac{\tilde{r}}{\tilde{R}} + \cot^{-1} \frac{\xi - 1}{\alpha} \right) & \xi \geq \xi_c \end{cases} \quad (4)$$

with a normalization condition

$$\int_{\tilde{R}}^{\tilde{D}} \tilde{\rho}(\tilde{r}) \tilde{r} d\tilde{r} = \xi \quad (5)$$

A related quantity of interest is the counterion integrated charge in a cylinder of varying radius, which is, using Gauss’ law,

$$\begin{aligned} \frac{\lambda(\tilde{r})}{\lambda} &= 1 + \frac{\tilde{r} u'(\tilde{r})}{2\xi} \\ &= 1 - \frac{1}{\xi} \left[1 + \alpha \cot \left(\alpha \ln \frac{r}{R} + \cot^{-1} \frac{\xi - 1}{\alpha} \right) \right] \end{aligned} \quad (6)$$

Electroneutrality imposes that $\lambda(\tilde{D}) = \lambda$ while $\lambda(\tilde{R}) = 0$.

The choice of units ($2\pi l_B \sigma^2$) to measure the density is of course not essential but proves convenient in that it will make contact densities at $r = R$ of order 1. In addition, the contact theorem²⁶ imposes that, in the limiting case of an isolated charged plate, the contact density is strictly fixed to unity: $\tilde{\rho} = 1$. For a given surface charge σ , the planar limit is obtained taking $R \rightarrow \infty$, with other parameters being kept constant. It thus corresponds to $\xi \rightarrow \infty$ but Ξ fixed, a thick cylinder case indeed ($\xi \gg \Xi^{1/2}$). However, as far as mean field is concerned, the difference between thick and thin cylinders is immaterial, so that we should soon check that $\tilde{\rho}(\tilde{R}) \rightarrow 1$ when $\xi \rightarrow \infty$ after having sent the boundary to infinity ($\Delta \rightarrow \infty$). The SC profiles to follow in section 3 are not endowed with the same property, since the functional forms of $\tilde{\rho}$ strongly differ in the thick and needle configurations.

For the most part, the interesting regime is that of $\xi > \xi_c$. In the large $\Delta = \log(D/R)$ limit, we then have $\cot(\alpha\Delta) \approx 1/(\pi - \alpha\Delta)$ and

$$\alpha \approx \frac{\pi}{\Delta + 1} \left(1 - \frac{1}{\xi - 1} \frac{1}{\Delta} \right) \quad (7)$$

which determines the behavior of $\tilde{\rho}$. From

$$\cot^{-1} \left(\frac{\xi - 1}{\alpha} \right) \approx -\alpha(\Delta + 1) \quad (8)$$

we get

$$\tilde{\rho}(\tilde{r}) = \frac{1}{\xi^2} \left(\frac{\tilde{R}}{\tilde{r}} \right)^2 \left[\frac{\frac{\pi}{\Delta + 1}}{\sin \left[\frac{\pi}{\Delta + 1} \left(\log \frac{\tilde{r}}{\tilde{R}} + \frac{1}{\xi - 1} \frac{\xi - 1}{\alpha} \right) \right]} \right]^2 \quad (9)$$

which holds for $\xi > 1$. Hence, the density in the $\Delta \rightarrow \infty$ limit³

$$\tilde{\rho}(\tilde{r}) = \frac{(\xi - 1)^2}{\xi^2} \left(\frac{\tilde{R}}{\tilde{r}} \right)^2 \left[1 + (\xi - 1) \log \frac{\tilde{r}}{\tilde{R}} \right]^{-2} \quad (10)$$

It appears that, for $\xi \leq 1$, $\tilde{\rho} = 0$ at all distances, which signals complete evaporation of counterions. In other words, a cylinder is only able to bind ions if the value of the Manning parameter is higher than unity. For $\xi > 1$, we further have

$$\int_{\tilde{R}}^{\infty} \tilde{\rho}(\tilde{r}) \tilde{r} d\tilde{r} = \xi - 1 \quad (11)$$

to be compared to eq 5. The evaporated fraction of counterions is therefore $1/\xi$. For large although not infinite values of Δ , the phenomenon remains, although, of course, a distance criterion is required to differentiate condensed from evaporated ions, since normalization (eq 5) always holds. To this end, a convenient inflection point criterion has often been used^{9,27,28} (see also, e.g., ref 29 for a related discussion with added salt): the integrated charge $\lambda(r)$ plotted as a function of $\log r$ shows an inflection point precisely where

$$\log \frac{r_c}{R} = \Delta \left[1 - \frac{\cot^{-1} \alpha}{\alpha \Delta} \right] \quad (12)$$

which corresponds to $\lambda(r_c)/\lambda = 1 - 1/\xi$ and renders an effective integrated charge of $\xi - 1$. It follows directly that $r_c = R$ at $\xi = 1$ and for $\xi > 1$

$$\log \frac{r_c}{R} \approx \frac{\Delta + 1}{2} \left[1 - \frac{1}{\Delta(\xi - 1)} \right] \quad (13)$$

The distance r_c is often called the Manning radius.

For values of $\xi > 1$, ions will be condensed close to the surface of the cylinder, thus creating a cloud of charge with cylindrical symmetry that will screen the potential that other ions farther away perceive. Then, for a sufficiently large distance—beyond \tilde{r}_c —the integrated charge of the ion cloud and the cylinder is effectively $\xi = 1$ (Manning condensation) and the ions in the outer region will interact with an effective cylinder with charge equivalent to $\xi = 1$, which lies at the borderline of condensation. From the previous analysis, the fraction of ions condensed within r_c is f_M (Manning condensed fraction of ions), with

$$f_M = \frac{\xi - 1}{\xi} \quad (14)$$

and the condensed ions will form a cloud of charge $\xi - 1$. From eq 13, it appears that the Manning radius r_c for Δ very large, is close to $\Delta/2$ in logarithmic scale, and the normalization condition reads

$$\int_{\tilde{R}}^{\tilde{r}_c} \tilde{\rho}(\tilde{r}) \tilde{r} d\tilde{r} = f_M \xi = \xi - 1 \quad (15)$$

to be compared to eq 11 valid for infinite dilution.

On the other hand, to quantify the extension of the electric double-layer, it is also instructive to compute the distance at which the integrated charge is half the condensed charge (i.e., $\lambda(r)/\lambda = (\xi - 1)/2\xi$). From eq 6,

$$\log \frac{x_{1/2}^{\text{MF}}}{R} = \frac{1}{\xi - 1 + 2 \frac{\alpha^2}{\xi - 1}} \approx \frac{1}{\xi - 1} \quad (16)$$

This teaches us that the relevant length scale for the extension of the ionic profile is R , a much smaller scale than the Manning radius. The above expression is compatible with the known fact that, in the planar limit, the extension is given by the Gouy length μ . Indeed, when $R \rightarrow \infty$ so that $\xi \rightarrow \infty$, we get from eq 16 that $x_{1/2}^{\text{MF}} - R \propto R/\xi = \mu$.

For future comparison with simulation data, we also specify the behavior in the vicinity of the outer cylinder. From eq 4,

$$\xi^2 \left(\frac{D}{R} \right)^2 \tilde{\rho}(r) \approx \left(\frac{D}{r} \right)^2 \left[1 - \log \frac{r}{D} \right]^{-2} \quad (17)$$

Conversely, in the vicinity of the charged cylinder when the Manning parameter approaches the critical value, i.e., $\xi \rightarrow \xi_c$, we see from the transcendental eq 3 that, for $\xi = \xi_c^+$, $\alpha \rightarrow 0$, thus yielding

$$\xi_c^2 \tilde{\rho}(\tilde{r}) = \left(\frac{\tilde{R}}{\tilde{r}} \right)^2 \frac{1}{\left[\Delta + 1 - \log \frac{\tilde{r}}{\tilde{R}} \right]^2} \quad (18)$$

which gives a nonvanishing value for the density at a contact of Δ^{-2} for the density. A similar approach to the one performed for $\xi > \xi_c$ renders the same result for $\xi = \xi_c^-$. Note that the value at contact is strongly dependent on the log of the box size.

In the following analysis, the results displayed do not depend on the value chosen for the valency q of counterions, which will therefore not be specified, since it only matters through $\xi \propto q$ and $\Xi \propto q^3$.

3. STRONG COUPLING

3.1. Leading Order Behavior (SC-0). In the strong-coupling large Ξ limit, at fixed ξ , the ratio $a'/R \propto \Xi/\xi^2$ becomes large: this is another way to define the needle limit. Hence, the typical distance between particles becomes large compared to the radial distance they explore, and to leading order, the same single particle picture as in the planar geometry^{13,14} does hold.⁹ The ion–ion interactions become subdominant compared to the rod-ion term, and the counterion profile is thus given by the exponential of the bare cylinder logarithmic potential. This means that^{9,20} $\rho_0(r) \propto r^{-2\xi}$. The subscript 0 refers to the dominant order in a large Ξ expansion. This functional form cannot be normalized for $\xi \leq 1$ —we consider here the infinite dilution limit—yet another illustration of complete evaporation: the omitted prefactor is vanishing for $\xi \leq 1$, so that $\rho_0(r) = 0$. For $\xi > 1$, the previous profile is normalizable, though, and we have

$$\tilde{\rho}_0(r) = \frac{\rho_0(r)}{2\pi l_B \sigma^2} = f \frac{2(\xi - 1)}{\xi} \left(\frac{R}{r} \right)^{2\xi} \quad (19)$$

where we have assumed a fraction of condensed ions f , i.e.,

$$\int_{\tilde{R}}^{\infty} \tilde{\rho}(\tilde{r}) \tilde{r} d\tilde{r} = f \xi \quad (20)$$

We have seen in section 2 that $f = f_M = 1 - 1/\xi$ within mean field, a result that nevertheless holds beyond mean field.⁹ Taking $f = f_M = 1 - 1/\xi$, we write

$$\tilde{\rho}_0(r) = \frac{2(\xi - 1)^2}{\xi^2} \left(\frac{R}{r} \right)^{2\xi} \quad (21)$$

This is our leading prediction, denoted **SC-0** in the remainder, which turns out to differ from the result derived in refs 5 and 9 where the same form as eq 19 was considered but with the choice $f = 1$ that turns out to be incompatible with evaporation of a

non-vanishing fraction of ions. We will refer to the choice $f = 1$ as the SC-0 $f = 1$ form. We emphasize that the normalization relation does not specifically follow from the Wigner nor from the virial approach but is an essential requirement which, as we shall see, has been incorrectly accounted for in previous works.

It can be noted here that the typical distance into which the ions are confined is given by R , and does not depend on Ξ . More specifically, if we compute the distance corresponding to confinement of 50% of the ions, we get $x_{1/2}^{SC} = R2^{(2\xi-2)^{-1}}$, which exhibits a similar form as its mean field counterpart (eq 16). The coupling parameter Ξ is indeed absent, but the expression is compatible with the ground state requirement that $x_{1/2}^{SC} \rightarrow R$ when temperature vanishes, because then $\xi \rightarrow \infty$. For ξ of order 1 but larger than 1 to avoid complete evaporation, the relevant confinement scale is R . When ξ becomes large, we have noted that $x_{1/2} - R \rightarrow 0$, and more precisely $x_{1/2} - R \simeq R/\xi$, which, again, is the Gouy length $\mu \propto (ql_B\sigma)$, setting the confinement range in the planar case.

We note that the contact density following from eq 21 reads $\tilde{\rho}_0(R) = 2(\xi - 1)^2/\xi^2$, that is, exactly twice the mean field contact density found in eq 10. It also appears that it is not possible to recover the planar limit with its $\tilde{\rho}(R)$ constrained to unity by the contact theorem, since expression 21 only holds for small values of ξ^2/Ξ —this is the needle constraint—while the planar limit is met for $\xi \rightarrow \infty$ at fixed Ξ .

3.2. Correction to Leading Order (SC-1). Before comparing our SC-0 prediction to numerical data, we adapt the method used in refs 13 and 16 to compute the next term in the strong-coupling expansion. Such a procedure yields fundamentally different results than the virial approach of refs 20 and 21, since correction terms appear dressed with a different power of Ξ . These corrections have nevertheless not been worked out at the virial SC level in the present cylindrical geometry.

The starting point is to determine the ground state of the system, and to further consider the relevant excitations, those which contribute to the correction to SC-0. In other words, we should identify the excitations from the ground state that have the smallest energy cost, and we therefore first expand the interparticle potential assuming that the particle displacement \mathbf{X} ($\mathbf{X} = \mathbf{x} + z\hat{k}$ and $X^2 = x^2 + z^2$, \mathbf{x} being a vector in the plane perpendicular to the z axis) from its lattice position is small, i.e., $|\mathbf{X}| \ll a'$. We will assume that ground state positions are given by $\mathbf{r}_l = a'\hat{l}\hat{k}$, for $l \in \mathbb{Z}$, which corresponds to particles localized onto the z axis; see Figure 5. This is consistent with the needle limit where $R/a' \rightarrow 0$ for $\Xi \rightarrow \infty$. A more correct ground state is sketched in Figure 3, but for computing the desired correction to ρ_0 , it is sufficient to distort the true ground state into the simpler form shown in Figure 5; the same leading correction ensues.

The energy cost for a given configuration of ions reads (see section S1 in the Supporting Information for more details)

$$\beta\delta E = \xi \sum_j \log\left(\frac{\tilde{x}_j^2}{R^2}\right) + \frac{\xi^3}{\Xi^2} f^3 \sum_j \left\{ -\zeta(3)\tilde{x}_j^2 + \frac{1}{2} \sum_{l \neq j} \frac{\tilde{x}_l \tilde{x}_j}{|j-l|^3} \right\} + \xi f \sum_j \left\{ 2\zeta(3)\frac{z_j^2}{a'^2} - z_j \sum_{l \neq j} \frac{z_l}{a'^2 |j-l|^3} \right\} \quad (22)$$

where ζ is the Riemann zeta function ($\zeta(3) \simeq 1.202$). In all formulas and provided that the system size is big enough, we consider $f = 1 - 1/\xi$. We however leave the fraction f apparent, for it becomes a nontrivial function of ξ , coupling parameter, and confinement when finite-size effects do matter (see section 6).

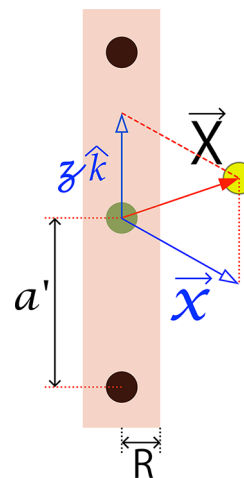


Figure 5. A $R \rightarrow 0$ approximation of the ground state for the cylinder system in the needle limit. The length a' should account for ionic evaporation, so that it is defined as $a' = q/(\lambda f)$, with $f = 1 - 1/\xi$. Hence, $R/a' = \xi^2 f/\Xi = \xi(\xi - 1)/\Xi$.

The form of eq 22 calls for some comments before its use in the Wigner strong-coupling machinery.^{13,16} When considering separately the displacements of particles along the rod (variables z), or perpendicularly (variables \mathbf{x}), a dual localization phenomenon appears. The coupling parameter Ξ governs the localization of ions onto the rod, which was already clear from the relation $R/a' \propto \xi^2 f/\Xi < \xi^2/\Xi$. It is not coupled to the z degree of freedom, so that, even at very large Ξ , the essentially one-dimensional system of condensed counterions may be fluid. It is then the Manning parameter ξ that governs crystallization along the rod direction, and is thus the parameter coupled to the z degree of freedom in eq 22. Another way to recover this conclusion is to compute the coupling (plasma) parameter corresponding to ions on a line, with interparticle distance a' : we get $q^2 l_B/a'$, which is equal to $\xi - 1$. We therefore expect a one-dimensional transition for large values of ξ , at large Ξ such that the needle scenario holds ($\Xi \gg \xi^2$). In all of this discussion, it is implicitly understood that the ions are typically confined, radially wise, in a sheath of extension R around the cylinder. This is indeed the case in the SC regime as well as within mean field; see the discussion in section 3.1.

Considering the Boltzmann weight constructed from the energy (eq 22), we fix one tagged particle at a given position \mathbf{x}_0 and integrate over the remaining particles, in the spirit of the procedure worked out in refs 13 and 16: $\rho(\mathbf{x}_0) = C\langle \delta(\mathbf{x} - \mathbf{x}_0) \rangle$, with C being a normalization constant. After some algebra detailed in section S1 of the Supporting Information and under the proper normalization condition (eq 11), we arrive at

$$\tilde{\rho}_1(r) = 2f \frac{(\xi - 1)}{\xi} \left(\frac{R}{r}\right)^{2\xi} \times \left\{ 1 + \zeta(3) \frac{\xi^5}{\Xi^2} f^3 \left[\left(\frac{r}{R}\right)^2 - \frac{\xi - 1}{\xi - 2} \right] \right\} \quad (23)$$

subsequently referred to as SC-1. We will discuss later the limit of validity of the above expansion. It should be emphasized that the profile (eq 23) is an expansion in r , which does not hold up to ∞ . This poses a problem for normalization, since the neglected higher order terms become prevalent for $\xi < 2$, and explain why eq 23 can only be normalized for $\xi > 2$. This leads

to the conclusion that, while the zeroth order term ρ_0 may give a reasonable profile for small values of ξ (to be precisely defined in section 5), the correction ρ_1 is deficient for $\xi < 2$.

3.3. A Single Particle Variant. There is an alternate seminumerical treatment to the strong-coupling problem. Within the range of high values of ξ and Ξ , such that $\xi^2 f/\Xi \ll 1$, we fix the ions at their ground state positions, and compute the energy cost if one particle (and only one) is shifted perpendicularly from this structure, consistent with the single particle picture in the strong-coupling regime. The density profile is then

$$\tilde{\rho}(r) = \left(\frac{R}{r}\right)^{2\xi} \exp\left[-2\xi f \sum_{j>0} \left(\frac{1}{\sqrt{j^2 + \left(\frac{r\xi}{\Xi}\right)^2}} - \frac{1}{j}\right)\right] \quad (24)$$

up to a normalization constant. The series involved in the calculation has no known closed form. For large distances,

$$\sum_{j>0} \left(\frac{1}{\sqrt{j^2 + x^2}} - \frac{1}{j}\right) \approx -\log x + \text{const} \quad (25)$$

meaning that the large distance behavior is $\rho(r) \propto 1/r^2$, as is the case within mean field. The profile (eq 24) is, therefore, not normalizable when $\Delta \rightarrow \infty$. There is however a large range of upper cutoff distances where the resulting normalized expression (eq 24) is invariant close to the charged rod, so that the normalization problem can be in practice easily circumvented. Equation 24 can be viewed as an improved version of SC-0, and will be referred to as SC-0*. In particular, it reproduces the $r^{-2\xi}$ behavior in the vicinity of the charged rod.

4. MONTE CARLO SIMULATIONS

For the numerical computations, we will adapt Monte Carlo sampling to the cell geometry, and impose periodic boundary conditions along the main axis of the cylinder (z), taking due account of the long range of Coulomb potential. In the xy plane, the counterions are confined between the cylinder (R) and the outer shell (D). There have been extensive reports on numerical implementations for the calculation of the potential for periodic boundary conditions under a number of geometries.^{30–34} For the 1D periodic case, the Lekner–Sperb sums³² have been the standard method to account for all the electrostatic contributions. The evaluation of such sums is numerically expensive, and requires in particular the calculation of an important number of terms for short distances. Here, we introduce a novel analytic formulation deduced from the Poisson–Jacobi transformation, as proposed in ref 35. It is simple to implement and is free of divergences in all ranges of interparticle distances. The resulting energy is based on the Ewald separation of the potential in a term that converges quickly in real space and another that converges quickly in Fourier space. Details are presented in sections S2 and S3 in the Supporting Information.

The potential energy of the system can be expanded as

$$U = U_R + U_F + U_C + U_S \quad (26)$$

Each of the terms are written in terms of two conveniently defined variables, ρ_{ij} the distance between the particles' positions projected to the plane perpendicular to the z axis and $z_{ij} = z_i - z_j$; here L_z is the length of the box along the periodic direction which is naturally chosen as the cylinder axis z .

$$U_R = \frac{1}{4\pi\epsilon\epsilon_0} \times \sum_{i=1}^{N-1} \sum_{j=i+1}^N q_i q_j \left[\sum_n \frac{\text{Erfc}(\alpha(\rho_{ij}^2 + (z_{ij} + L_z n)^2)^{1/2})}{(\rho_{ij}^2 + (z_{ij} + L_z n)^2)^{1/2}} + \frac{1}{L_z} \begin{cases} 0 & \rho_{ij} = 0 \\ -\gamma - \log(\alpha^2 \rho_{ij}^2) - E_1(\alpha^2 \rho_{ij}^2) & \rho_{ij} > 0 \end{cases} \right] \quad (27)$$

where q_i is the charge of particle i , $\alpha > 0$ is a parameter chosen for convergence, γ is the Euler–Mascheroni constant, $\text{Erfc}(x)$ is the complementary error function, and $E_1(x)$ is the exponential integral as defined in section S3 in the Supporting Information.

$$U_F = \frac{1}{2\pi\epsilon\epsilon_0 L_z} \sum_{i=1}^{N-1} \sum_{j=i+1}^N q_i q_j \sum_{k>0} K_0\left(\frac{k^2}{4\alpha^2}, \alpha^2 \rho_{ij}^2\right) \cos(k \cdot z_{ij}) \quad (28)$$

where $k = 2\pi n/L_z$ for $n \in \mathbb{Z}$ and $K_0(x, y)$ is the incomplete Bessel function. Further references for the evaluation of this function can be found in refs 36 and 37

$$U_C = -\frac{\lambda}{2\pi\epsilon\epsilon_0} \sum_{i=1}^N q_i \log\left(\frac{\rho_i}{R}\right) \quad (29)$$

with λ being the linear charge density of the cylinder ($\sigma = \lambda/(2\pi R)$). Notice that the cylinder is located at the origin of coordinates.

$$U_S = \frac{1}{4\pi\epsilon\epsilon_0} \left(\sum_{n>0} \frac{\text{Erfc}(\alpha L_z n)}{L_z n} + \frac{1}{L_z} \sum_{k>0} E_1\left(\frac{k^2}{4\alpha^2}\right) - \frac{\alpha}{\sqrt{\pi}} \right) \times \left(\sum_{i=1}^N q_i^2 \right) + \frac{\lambda^2 L_z}{8\pi\epsilon\epsilon_0} (\gamma + \log(\alpha^2 R^2)) \quad (30)$$

The previous expression for the energy is free of divergences for any value of $\rho_{ij} = 0$, and since the particles are bounded to the cell, we have $0 < \log(\rho_i/R) < \Delta$. All simulations were taken with a number of particles that ranged between 300 and 1000, and ran typically over 10^7 steps.

In the problem under scrutiny, finite-size effects are important and logarithmic in D/R , which requires very large system sizes and consequently precludes standard sampling methods. To circumvent this difficulty, we use the centrifugal sampling technique⁹ which consists of writing the partition function with more convenient log variables, $Y = \log(r/R)$. Then, the partition function

$$\mathcal{Z} = C_0 \int_{V^N} d\mathbf{r}^N dz^N \exp(-\beta U(\mathbf{r}^N, z^N)) \quad (31)$$

transforms to

$$\mathcal{Z}' = C'_0 \int_{V'^N} d\theta dY^N dz^N \exp(-\beta U(\mathbf{r}^N, z^N)) + 2 \sum_i Y_i \quad (32)$$

which redefines the energy into

$$U'(Y^N, \theta^N, z^N) = U(\mathbf{r}^N, z^N) - \frac{2}{\beta} \sum_i Y_i \quad (33)$$

The calculation of the interparticle potential energy requires one to know the Cartesian coordinates of the particles; hence, the transformation of coordinates has to be performed each time a particle moves. For the latter choice of variables, we can choose a Monte Carlo step size of $(\Delta Y, \Delta \theta, \Delta z)$ such that, for short distances ($Y \approx 0$), a displacement of Δr is at most of a Gouy length. Equivalently,

$$\Delta Y = \log \left[\frac{R + \mu}{R} \right] \approx \frac{1}{\xi} \quad (34)$$

For the sake of efficient equilibration, it proves useful to distinguish between two kinds of ions in our system. Bounded ions are constrained to a shell measured in R units, as discussed in sections 2 and 3.1. Their unbounded counterparts cover a region beyond the Manning radius (r_c) where the average interparticle spacing is much larger than the electrostatic correlation length l_b , hence forming a weakly coupled gas. From mean field (eq 13), we expect the location of the Manning radius near $\Delta/2$ in log units. This question will be further explored when presenting our results. As a part of the equilibration process, particles have to be exchanged between the two populations. To this end, we propose to move one particle from Y to $Y' = \Delta - Y$. Performing twice such a move will return a particle to its original position. Therefore, detailed balance is preserved by choosing a fixed probability p ($p \sim 10^{-4}$) to select this type of particle exchange move over a regular one. The attempt is then accepted employing the usual Metropolis criterion. Such an approach guarantees proper equilibration independently of any chosen initial condition for the counterions. This is particularly important for the study of finite size systems at large coupling, as algorithms with only standard moves (including the original centrifugal sampling method) will not correctly sample the configuration space.

5. PROFILES, CORRELATIONS, AND ORDER PARAMETER

We present in this section the bulk of our results. A large system has been simulated, in order to get rid of finite-size effects, that shall be studied separately but in a more cursory fashion in section 6. We start by validating our simulation procedure against known results. To this end, two features can be used. We can first check that, for small Ξ , the mean field (MF) expressions are recovered, and also that, at arbitrary Ξ , the condensation scenario coincides with the MF one.⁹

5.1. Counterion Condensation/Evaporation. We begin by the condensation phenomenon. For $\xi < 1$, all ions dilute away when $\Delta = \log(D/R)$ increases. For $\xi > 1$, a fraction f of ions remain condensed in the vicinity of the charged rod. This can be seen in Figure 6, which shows the integrated line charge $\lambda(r)$ in a cylinder of varying radius r , as introduced in the mean field section 2. By definition, $\lambda(R) = 0$, while electroneutrality requires $\lambda(D) = \lambda$. The ionic atmosphere is more bound to the rod as the coupling parameter Ξ increases, and the profile then strongly departs from MF. Further from the rod, ionic correlations decrease as a consequence of the lower ionic density, to such an extent that the tail of the ionic profile is described by mean field. This is why, in the right-hand side of the figure, the different Ξ curves collapse, and coincide with the MF form. The inflection point property, that is clearly visible, hence takes place at a point that is Ξ independent, for which mean field results apply.⁹ This provides the rationale for the two-fluid picture (bound ions before the inflection point,

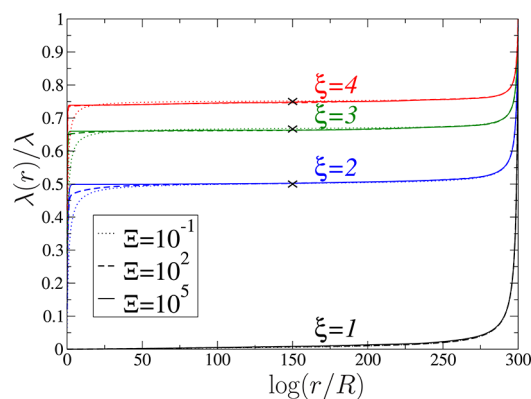


Figure 6. Carlo measured cumulative density of particles for $\Delta = 300$ as a function of the logarithmic distance $\log(r/R)$, for $\Xi = 10^{-1}$, 10^2 , and 10^5 and $\xi = 1, 2, 3$, and 4 . The crosses drawn close to $(\Delta/2, f = 1 - 1/\xi)$ are the expected locations of the inflection point, at the Manning radius r_c given by eq 13. The mean field prediction (eq 6) superimposes to the $\Xi = 0.1$ results.

unbound beyond) that is often used for polyelectrolyte but that is quite specific to the salt-free case.²⁹ Note also that, to observe the Manning condensed fraction $f = f_M = 1 - 1/\xi$ as in Figure 6, exponentially large box sizes are required. We come back to this point in section 6. Our results reproduce previously reported data.^{5,9} For instance, extracting the inflection-point location from plots such as Figure 6, we always obtain a condensed fraction that is extremely close to $f_M = 1 - 1/\xi$; see Figure 7. Figures 6 and 7

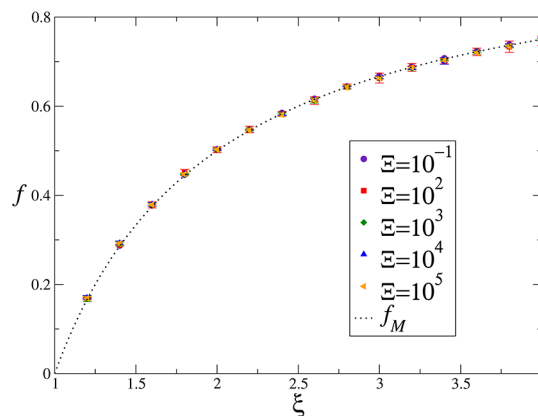


Figure 7. Condensed fraction of ions as a function of the Manning parameter ξ for values of Ξ in mean field and in the strong-coupling regime ($\Delta = 300$).

justify the normalization choice made in section 3, that led to eqs 21 and 23. Indeed, the strong-coupling profiles are meant to describe the ionic atmosphere in the vicinity of the charged rod, an atmosphere that is deprived, over an exponentially large distance range, from the ions that lie in the vicinity of the confining border. This results in the plateau of Figure 6, at a value that does not correspond to full neutrality. Note that the term “vicinity” here should be taken in the broad sense, since it can be seen in Figure 6 that $\lambda(r)$ changes to reach full neutrality $\lambda(D)/\lambda = 1$ in the range where $260 < \log(r/R) < 300$, so that r changes by a factor $e^{40} \approx 10^{17}$.

5.2. Density Profiles. Having validated our normalization procedure from integrated profiles, we turn with Figure 8 to a more precise analysis of the profiles themselves close to the charged cylinder. As expected, the small Ξ results coincide with

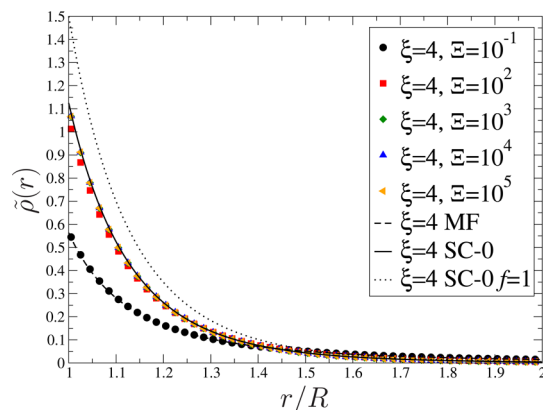


Figure 8. Radial density profile for different values of Ξ and fixed $\xi = 4$ for $\Delta = \log(D/R) = 300$. The symbols show the Monte Carlo results. The lines are for the mean field (MF) result and our SC-0 (strong coupling to leading order) analytic solution (eq 21). The SC-0 $f = 1$ prescription of refs 5 and 9 is shown by the upper dotted curve. The reduced density is defined as $\tilde{\rho} = \rho / (2\pi l_B \sigma^2)$.

their mean field form; see the $\Xi = 0.1$ curve. On the other hand, when Ξ is large enough and exceeds 10^2 , all profiles collapse onto the SC-0 prediction, eq 21. As anticipated, the mean field contact value [$\tilde{\rho}(R) = 9/16 \approx 0.56$ for $\xi = 4$] is half its strong-coupling counterpart. A more thorough analysis of the contact density will be presented in section 5.6, in conjunction with the study of the corrections to SC-0 and the test of the SC-1 formulation.

The algebraic form of SC-0 is better appreciated in the logarithmic plot of Figure 9, which shows that the $\Xi = 10^2$

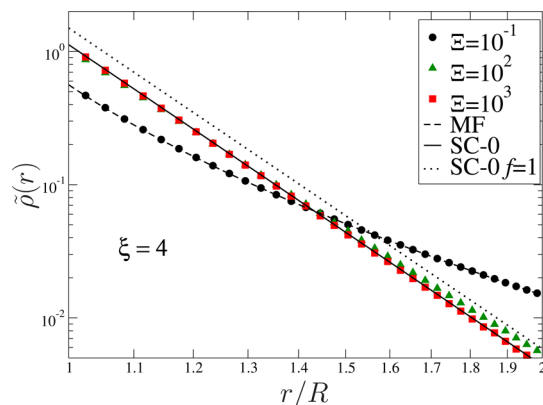


Figure 9. Log–log plot of the radial density profile for different values of Ξ with fixed $\xi = 4$. The symbols display the Monte Carlo results. The dashed line indicates the mean field (MF) prediction coinciding with the $\Xi = 10^{-1}$ Monte Carlo data. The continuous curve is for the SC-0 strong coupling to leading order analytic solution (eq 21) which superimposes to the $\Xi = 10^3$ data and partially with the $\Xi = 10^2$ points, and finally, the dotted curve is for the SC-0 $f = 1$ formula of refs 5 and 9.

points tend to depart slightly from SC-0 for $r > 1.6R$, while those for $\Xi = 10^3$ are in excellent agreement with the prediction (eq 21). As explained above, eq 21 is a double expansion, first in large Ξ and second in small distances. It therefore does not hold up to arbitrary large r , and we will comment further on the large distance behavior in section 5.3.

Consistently with the integrated charge plateau of Figure 6, the $f = 1$ normalization of refs 5 and 9 does not fit with the numerical data; see the upper dotted curve in Figure 8. This

phenomenon is all the more pronounced as the Manning parameter is low; see Figures 10 and 11. On the other hand, the

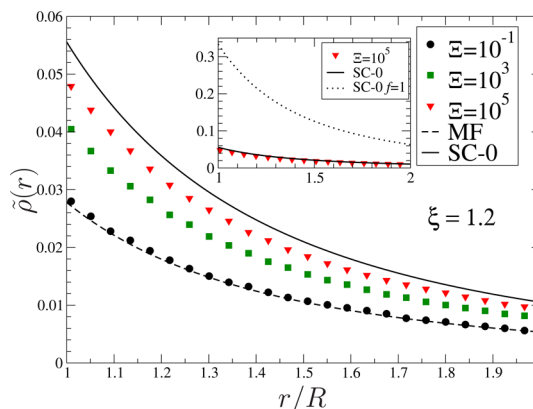


Figure 10. Same as Figure 8 where the SC-0 $f = 1$ prediction of refs 5 and 9 is shown by the dotted curve in the inset.

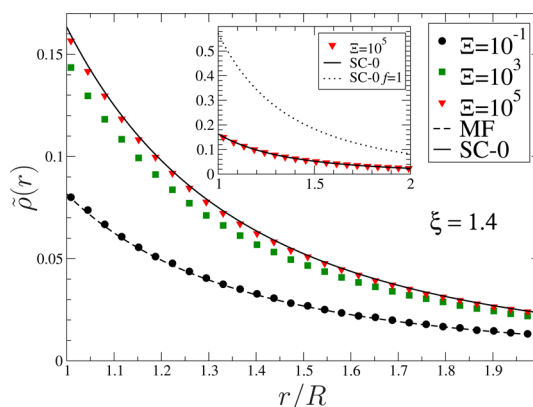


Figure 11. Same as Figure 10, for $\xi = 1.4$.

SC-0 eq 21 for $f = 1 - 1/\xi$ provides a reasonable profile when Ξ is large enough and ξ is not too close to unity: the agreement in Figure 11 is correct, and better than that in Figure 10. This was expected, since our SC approach is an expansion in the vicinity of the ground state of the system, and therefore better when, in addition to Ξ , ξ is large enough. It even comes as a surprise that we can get semiquantitative agreement for such low values as $\xi = 1.2$ and good agreement for $\xi = 1.4$.

5.3. Universal Crossover to Mean Field at Large Distances.

The decay of the ionic profile with distance r has led various authors to surmise that mean field should hold at large enough distances.^{38–40} Indeed, one may define a local coupling parameter $\Xi(r)$ from the ratio of Bjerrum length to the typical distance \bar{d} between counterions at a given distance r . With $\rho(r)$ of order unity, we expect $\Xi(r) \propto \rho(r)^{1/3}$, which should bring the profile into the mean field region $\Xi(r) \ll 1$ when $r \rightarrow \infty$. Previous works go in that direction^{14,41} but remained at the level of integrated quantities.⁹ Here, we are interested by the density profiles, and emphasize that explicit checks of this expectation are in general difficult to perform, due to the fact that the distances one should be able to probe can be very large. Our present study is nevertheless particularly well suited for investigating such an effect, due to the large systems considered.

We start by considering infinite system sizes $\Delta \rightarrow \infty$. We note here that, if mean field holds at large r , then the profiles should not only become independent of Ξ but also on ξ

(attention should be paid here to the difference between the normalized profile $\tilde{\rho}$ and the original one $\rho \propto l_B \sigma^2 \tilde{\rho}$). This is a property of the relation 10 which gives asymptotically that $\tilde{\rho}(r) \propto \xi^{-2} (R/r)^2 / \log^2(r/R)$. Going back to the initial profile, we get $\rho(r) \propto l_B^{-1} r^{-2} / \log^2(r/R)$, for all values of ξ . This universality is illustrated in Figure 12, where the curves for different ξ and for

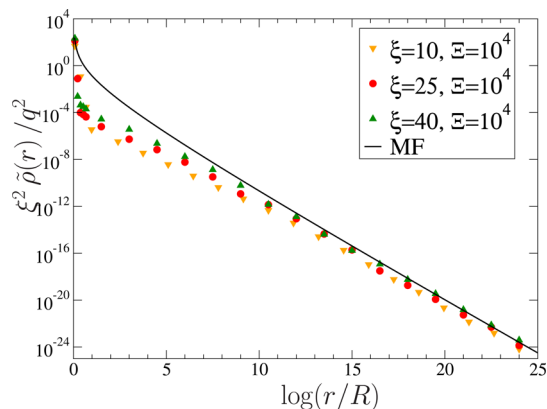


Figure 12. Plot of $\xi^2 \tilde{\rho}(r) / q^2 = 2\pi l_B R^2 \rho$ as a function of radial distance, for $\Delta = 300$. As in other figures, the symbols are for the Monte Carlo data. The mean field prediction, which holds for the three values of ξ , has been added (line).

large couplings asymptotically coincide with the MF expression. The figure also highlights the fact that the distances needed to evidence the MF form are quite large, $r/R > e^{10} \simeq 2 \times 10^4$. The figure corresponds to $\Delta = \log(D/R) = 300$, so that, for the range of distances displayed, the behavior is very close to its $\Delta \rightarrow \infty$ limit. A single mean field curve appears in Figure 12, since, for the range of distances shown, the MF solutions for the different ξ values differ only for very small r .

Figure 12 revealed that the mean field tail is visible for small densities/large distances only. On closer inspection, it appears that the departure from the SC behavior which holds at small r is quite sharp, as shown in Figure 13: the algebraic

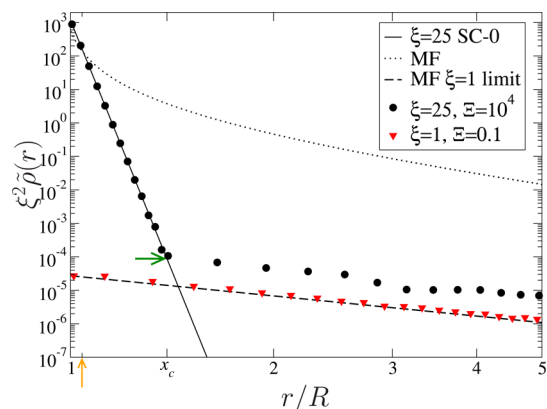


Figure 13. The radial density for different values of Ξ , ξ , and $\Delta = 300$. The dashed lines indicate respectively the mean field (MF) profile for $\xi = 1$ and the dotted curve for $\xi = 25$. The strong coupling to leading order analytic solution (SC-0) is presented in the solid curve. The right arrow indicates the crossover location ($x_c \approx 1.38$), and the up arrow indicates the location of a Gouy length from the surface of the cylinder.

profile in $r^{-2\xi}$ holds up to $r/R \simeq 1.4$. It abruptly evolves into another form for larger distances, a form that is still far from the MF expression (upper dotted curve) but closer to the critical

$\xi = 1$ mean field curve (which of course is fully compatible with the MC results at the low $\Xi = 0.1$). The latter remark provides an approximate means to compute the crossover point r_c where SC-0 ceases to hold: we simply equate the SC-0 (eq 21) and MF- $\xi = \xi_c$ density value at contact (eq 18) forms to get

$$\log x_c = \frac{1}{\xi} \log[\sqrt{2} f_M \Delta] \tag{35}$$

where $x_c = r_c/R$. We learn here that the dominant form of the crossover point behaves as

$$x_c \propto \Delta^{1/\xi} \tag{36}$$

The dependence on the Manning parameter agrees qualitatively with Figure 12 where x_c decreases upon increasing ξ . One interesting trait of finite Δ on the distribution of ions is that at the critical Manning transition parameter ($\xi = \xi_c$) the value of the contact density at the surface of the cylinder is not zero but Δ^{-2} , which can be a small quantity, thus providing the order of magnitude of the density that must be reached before a mean-field-like behavior can emerge.

A complementary means to illustrate the universality of MF behavior at large distances is provided in Figure 14, which is

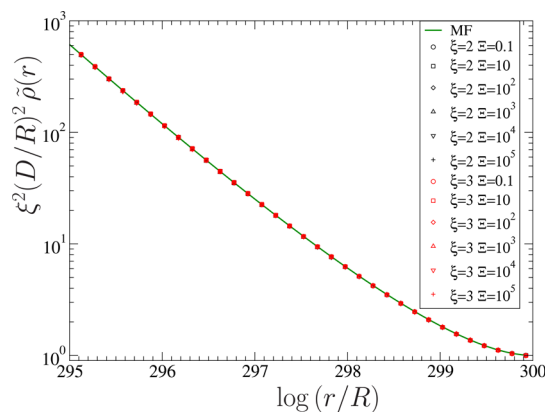


Figure 14. Profile near the edge of the box, for $\xi = 2$ or 3 , $\Delta = 300$, and values of Ξ in all regimes. The solid curve corresponds to the mean field eq 17.

explicitly governed by finite size effects. We know from section 2 that the density in the vicinity of the confining cylinder at $r = D$ is given by eq 17. The data collapse displayed in Figure 14 is remarkable, and shows that the ξ and Ξ independent mean field physics is at work in the tail of the profile.

5.4. Order Parameter for the Evaporation Transition.

The mean inverse distance is a parameter that can conveniently be used to see the transition from the condensed to the decondensed phase for which, a priori, we expect a critical change around $\xi = 1$. Following refs 5 and 9, we therefore consider the order parameter S_1 as $N^{-1} \sum_{i=1}^N \overline{r_i^{-1}}$, where the overline refers to the Monte Carlo time average at equilibrium. In other words, we have

$$S_1 = \frac{1}{2\pi\xi} \int d\vec{r} |\vec{r}|^{-1} \tilde{\rho}(\vec{r}) \tag{37}$$

Discarding box size effects (assuming $\Delta \rightarrow \infty$), S_1 behaves as

- Mean field (MF, eq 10)

$$S_1^{(MF)} = \frac{\xi - 1 - e^{1/(\xi-1)} E_1\left[\frac{1}{\xi-1}\right]}{\xi^2} \tag{38}$$

- Strong coupling to leading order (SC-0, eq 19)

$$S_1^{(\text{SC-0})} = f \frac{2(\xi - 1)}{\xi(2\xi - 1)} = \frac{2(\xi - 1)^2}{\xi^2(2\xi - 1)} \quad (39)$$

Figure 15 shows the results from the Monte Carlo simulations taken with values of ξ and Ξ in all ranges. S_1 vanishes for

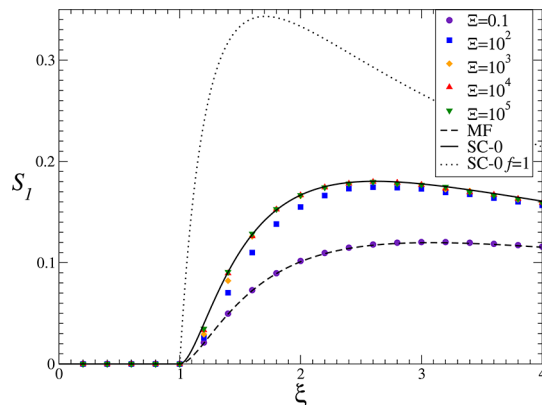


Figure 15. Order parameter S_1 (mean inverse distance from the cylinder) as a function of the Manning parameter ξ , for different couplings Ξ and $\Delta = 300$. The lines indicate the mean field (MF, eq 38) and strong coupling to leading order (SC-0, eq 39) analytic solutions. The upper dotted curve corresponds to the analytical prediction, eq 68, in ref 9.

$\xi < 1$, since all ions dilute away from the charged rod, while $S_1 \neq 0$ when $\xi > 1$ (here, we discard the small correction to unity that results from the fact that Δ is not infinite). As before, the agreement with mean field is excellent at $\Xi = 0.1$, and equally good is the consistency with SC-0 for large Ξ (10^3 , 10^4 , and 10^5). The data at $\Xi = 10^2$ appear quite close to the strong-coupling limit but exhibit some discrepancy. These data further illustrate the relevance of normalizing the profile with $f = 1 - 1/\xi$ and not $f = 1$; see the upper dotted curve.

5.5. Toward the Ground State: Crystallization Scenario.

After having investigated the properties of the density profiles perpendicular to the charged rod, we now address the question of the correlations along the rod (z direction), through the computation of the essentially one-dimensional pair correlation function g_z of bounded particles along the z -axis. The normalization of this object was done with respect to the number of ions close to the surface of the cylinder, thereby considering in the calculation only those ions present between two concentric cylindrical shells at $r = R$ and $r = R + 10\mu$. Normalization ensures that $g(z) \rightarrow 1$ at large z .

The results for g_z are presented in Figures 16 and 17. They shed light on the crystallization phenomenon that takes place here and on the asymmetric roles played by the two parameters Ξ and ξ . Figure 16 shows that, beyond a certain value, the correlations along the cylinder no longer depend on Ξ . This was expected from the dual localization argument developed in section 3.2. A large Ξ confines the ions in the vicinity of the charged rod, but their interaction along z is governed by ξ . If the latter quantity is small, we face an effective one-dimensional liquid, that is mildly modulated in Figure 16. In passing, this figure illustrates that the number of particles taken for the simulations (300) is actually sufficient for our purposes: identical results are obtained with $N = 1000$. Upon increasing ξ , crystallization occurs along the cylinder, as hinted in Figure 17,

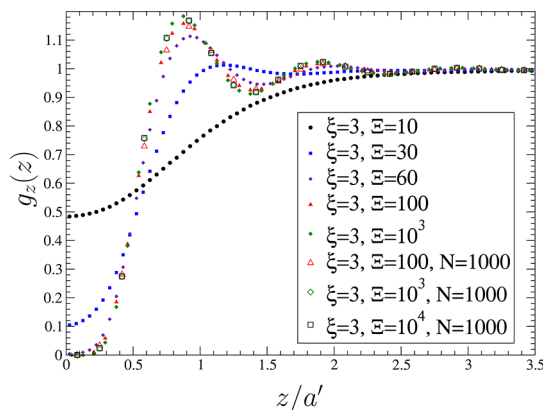


Figure 16. Normalized pair correlation function along the cylinder for $\xi = 3$ and different values of Ξ . The number of particles is $N = 300$ unless specified in the legend, and $\Delta = 300$.

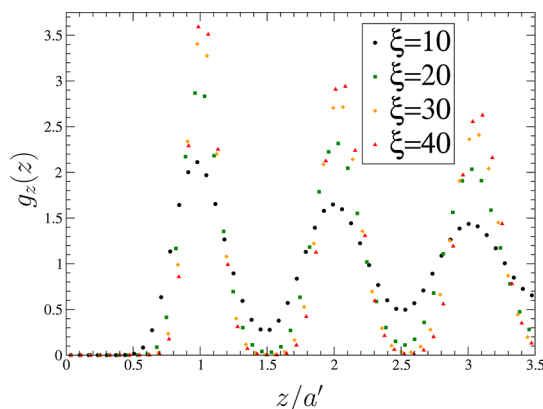


Figure 17. Pair correlation function along the z -axis for different values of ξ and $\Xi = 10^4$, and $\Delta = 300$. The number of particles is $N = 300$ unless specified in the legend.

where we recover the length scale a' as the correct measure of interparticle distances along z .

From the form of eq 22 and in particular the harmonic energy term in z , we expect that the first peak of g_z will present approximate Gaussian shape. Under this assumption, the width of the peak can be read directly in eq 22 to be

$$\delta_z \propto (\xi f)^{-1/2} \quad (40)$$

From Figure 17, we can extract δ_z performing a Gaussian fit of the first peak. The resulting width is shown in Figure 18, which gives credit to the naive estimation and shows a very good agreement with the linear trend expected for δ_z as a function of $(\xi f)^{-1/2}$.

5.6. Ion Profile Close to the Cylinder and Correction to SC-0. We so far focused on quantities that were accurately described by the SC-0 form at large Ξ . Our goal is now to test the validity of improvements over this leading form (SC-1 or SC-0*). To this end, we plot in Figures 19–21 the quantity $r^{2\xi}\tilde{\rho}(r)$, that yields a horizontal line at the SC-0 level, which is a way to make deviations from SC-0 more apparent. The numerical data thereby obtained show an increase with r , compatible with a parabola, which is also the trend predicted by the SC-1 expression; see eq 23. However, obtaining a quantitative agreement requires considering large values of ξ , for the agreement displayed in Figure 19 is quite poor. The situation is better in Figures 20 and 21. We therefore come to the conclusion that the leading SC-0 behavior may hold for

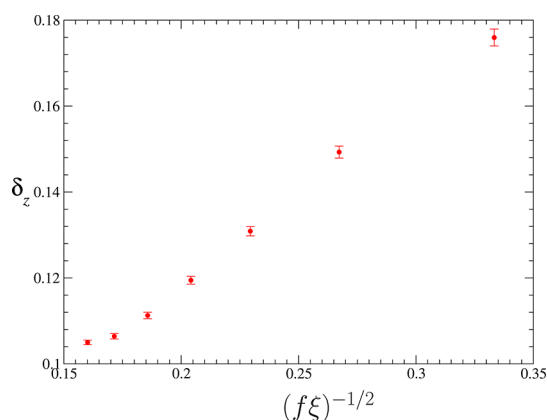


Figure 18. Width of the first peak of the numerical data for g_z in Figure 17. The simple argument giving eq 40 leads one to expect a straight line.

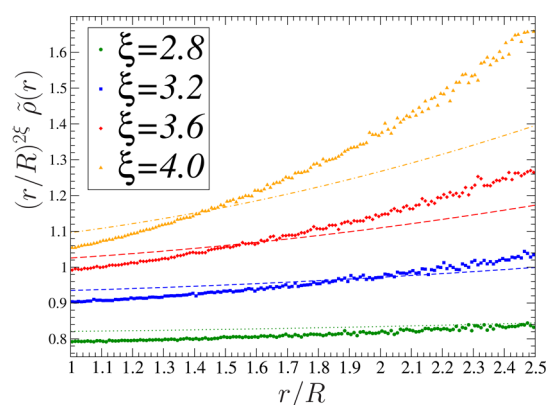


Figure 19. Radial ionic density for different values of ξ , $\Xi = 10^2$, and $\Delta = 300$. The dotted lines represent the analytic SC-1 result, eq 23.

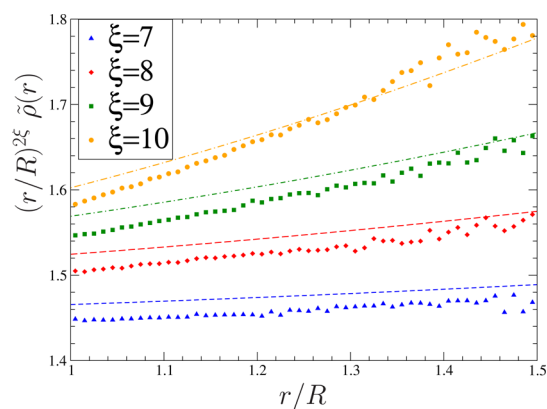


Figure 20. Same as Figure 19, for the same confinement but a higher coupling parameter $\Xi = 10^3$.

fairly low values of ξ , as discussed in section 3.1, while upon close inspection, the refinement SC-1 requires ξ to be large. This comes as no surprise, since ionic correlation does not enter the SC-0 form, while they are at the root of the SC-1 expression, derived assuming that all ions lie in the vicinity of their ground state position. As we have seen in section 5.5, this requires typically $\xi > 40$, and explains the poor agreement in Figure 19, while we have better consistency in Figures 20 and 21. In addition, we have reported in Figure 21 the results of the alternative improvement SC-0*, as given by eq 24. It seems that such a route improves upon SC-0 but also upon SC-1. However, some care is required in

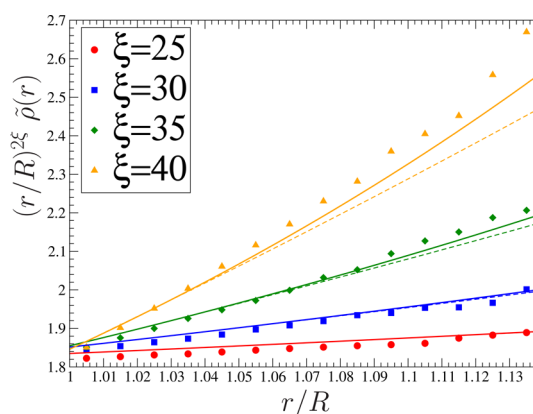


Figure 21. Same as Figures 19 and 20 for $\Xi = 10^4$. The solid curves represent the SC-0* prediction of eq 24.

interpreting the results: while SC-1 follows from an exact although perturbative statistical mechanics treatment, SC-0* remains at the single particle level, and is heuristic. Hence, SC-1 may be viewed as providing the next to leading contribution in the SC expansion of the ionic profile, which is not the case of SC-0*.

Note that, if ξ is too much increased at fixed Ξ , the needle requirement $\xi \ll \Xi^{1/2}$ may be violated at some point. This is not the case though with the data displayed in Figures 19–21. For instance, we have in the worst case $\xi/\Xi^{0.5} = 0.4$. It should also be noted here that, for large values of the Manning parameter, $(r/R)^{2\xi}$ becomes quite large for $r/R > 1$; hence, small fluctuations in the density profile induce large fluctuations in the graphed results.

To conclude this section, we report in Figure 22 the Monte Carlo measures for the density profiles at contact, together with

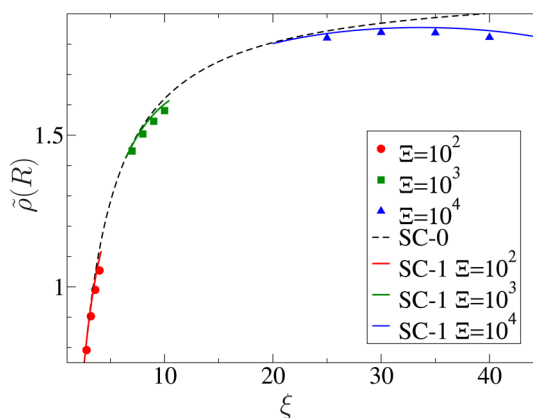


Figure 22. Contact density versus Manning parameter. As above, the symbols are for the Monte Carlo data and the lines for the analytical predictions. The dashed line displays the SC-0 form, which does not depend on Ξ . On the other hand, the SC-1 result following from eq 23 is Ξ dependent, and there are therefore three different branches (continuous curves) showing the corresponding expectation for the three values of Ξ studied.

the SC-0 and SC-1 predictions. While SC-0 expectedly gives the correct main trend of $\tilde{\rho}(R)$, it is seen that the Ξ dependent fine structure is well captured by SC-1. From the contact theorem, we also know that, at fixed Ξ , increasing further ξ ultimately leads to $\tilde{\rho}(R) = 1$. Such a trend is not visible in Figure 22, since the parameter range pertains to the needle limit, with constraint $\xi \ll \Xi^{1/2}$. Additionally, if the limit $\Xi \rightarrow \infty$

is taken first at arbitrary ξ , the SC-0 form becomes exact and we have $\tilde{\rho}(R) = 2(\xi - 1)^2/\xi^2$, twice the mean field expression as already noticed. Increasing next ξ , we finally get the large ξ result $\tilde{\rho}(R) \rightarrow 2$, exactly twice the planar result. It is this trend that is illustrated in Figure 22. To summarize, the limits of large ξ and large Ξ do not commute, and we can write

$$\lim_{\xi \rightarrow \infty} \lim_{\Xi \rightarrow \infty} \tilde{\rho}(R) = 2$$

$$\lim_{\Xi \rightarrow \infty} \lim_{\xi \rightarrow \infty} \tilde{\rho}(R) = 1$$

The latter equality may be written more generally as $\lim_{\xi \rightarrow \infty} \tilde{\rho}(R) = 1$ for all Ξ .

6. FINITE SIZE EFFECTS

In the previous section, we reported results for large system sizes, in order to have a universal fraction of condensed ions, and a clear-cut distinction between those ions that participate in the screening of the charged rod, and the decondensed one that lie in the vicinity of the confining border at $r = D$. These decondensed ions, which exist for all finite values of ξ , are the precursors of the ions which dissolve away when the system size is increased to infinity. For smaller systems, though, finite-size effects are very pronounced. This is illustrated in Figure 23,

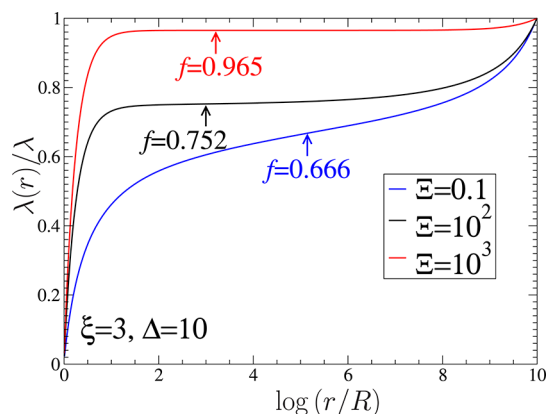


Figure 23. Cumulative density of particles for $\Delta = 10$. The inflection point is materialized by an arrow. The value of the condensed fraction, as given by the inflection point criterion, is indicated for each curve.

which differs significantly from its large Δ counterpart, Figure 6. Although $\Delta = 10$ in the figure is large enough to allow for discriminating condensed from decondensed ions, it is seen that the inflection point, which still provides a convenient cutoff for the partitioning, severely depends on the coupling parameter Ξ . In the mean field regime, the corresponding condensed fraction is still given by $f = f_M = 1 - 1/\xi$ (hence $2/3$ on the figure). Beyond mean field, the quantity increases with Ξ in a nontrivial fashion. Although the importance of finite-size effects has been clearly evidenced in refs 5 and 9, the finite-size study to follow is new.

A similar conclusion holds concerning the system size dependence; see Figure 24. For $\Delta > 50$ only do we get a condensed fraction that is close to its infinite dilution expression, $1 - 1/\xi = 2/3$ on the figure. A valid question is then to see if the strong-coupling prediction SC-0, eq 19, holds for the profile, with proper normalization f following from the inflection point rule. We can conclude from Figure 25 that this is indeed the case: the Monte Carlo data are in good agreement with our prediction, where the only *a priori* unknown is f , taken

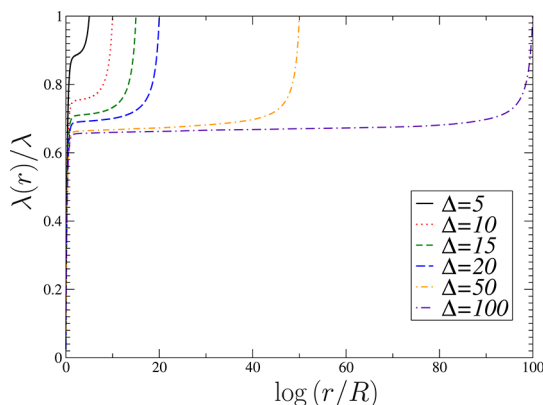


Figure 24. Build-up and size dependence of the integrated charge plateau for different values of Δ . Here $\xi = 3$ and $\Xi = 10^2$.

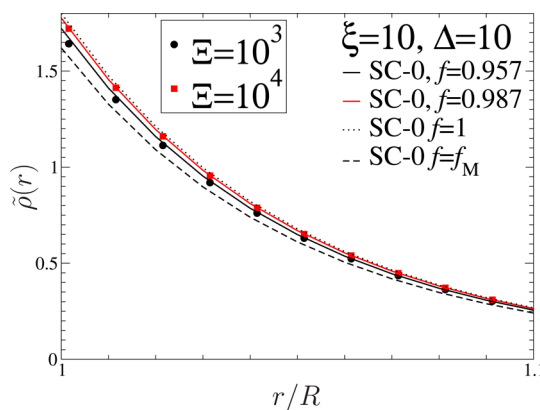


Figure 25. Density profile for $\xi = 3$, $\Delta = 10$, against the f -normalized strong-coupling prediction. The values of the condensed fraction f , used in the SC-0 form eq 19, are those which are read in Figure 23.

from Figure 23. The profiles are sandwiched between the limiting forms having $f = f_M = 1 - 1/\xi$, which appears to be a lower bound for the condensed fraction, and $f = 1$.

The remaining and final task is to quantify the dependence of f on system size Δ and coupling parameter, given that $f \simeq f_M$ when Δ is big enough; see Figure 7. To this end, it seems that one should distinguish the regimes of low Ξ where one essentially finds the mean field result f_M , see Figure 26, from the more strongly

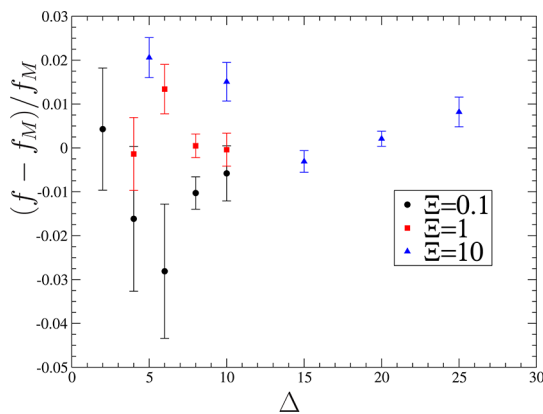


Figure 26. Condensed fraction of ions determined numerically using the inflection point criterion in the mean field and weakly coupled regime for $\xi = 3$.

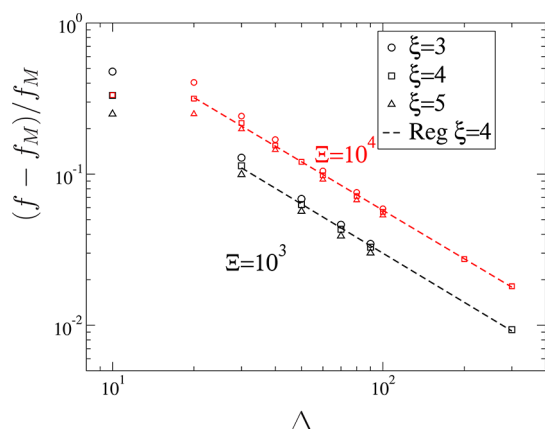


Figure 27. Condensed fraction under strong coupling, for $\xi = 3, 4,$ and $5,$ in a log–log plot where errors are less than the tick size. The dashed lines represent linear regressions which are summarized in Table 1.

correlated cases. Figure 27 shows that, in the latter case and for fixed coupling $\Xi,$ f decreases with confinement in such a way that

$$\frac{f - f_M}{f_M} \simeq \frac{\varepsilon}{\Delta^\gamma} \quad (41)$$

with ε and γ two dimensionless parameters reported in Table 1, and obtained from regressions on all data sets collected. A first

Table 1. Numerical Values for ε and γ from a Regression Performed Considering $(f - f_M)/f_M \simeq \varepsilon/\Delta^\gamma$ on Multiple Results^a

Ξ	ξ	ε	σ_ε	γ	σ_γ
10^2	3	12.5	2.2	1.99	0.08
10^3	3	7.52	0.06	1.198	0.003
10^4	3	16.0	0.8	1.23	0.02
10^2	4	2.5	0.2	1.57	0.05
10^3	4	3.5	0.2	1.02	0.02
10^4	4	7.6	0.5	1.06	0.02
10^2	5	0.16	0.13	1.0	0.2
10^3	5	4.1	0.1	1.096	0.007
10^4	5	8.4	0.2	1.100	0.005

^aThe quantities labeled σ refer to the standard deviations.

conclusion which can be drawn is that, except for too small Δ and $\xi,$ we have $\gamma \simeq 1.$ Quite expectedly, confining the system favors condensation. Second, the figure exhibits a departure from the $1/\Delta$ scaling on the left-hand side, where Δ is small. In this region, the quantity plotted becomes Δ independent, and turns out to reach its maximum possible value, i.e., $(\xi - 1)^{-1}$ corresponding to $f = 1.$ This is a hint that too small systems (say below some Δ_l) do not allow for evaporation to set in. For $\Delta > \Delta_l,$ $\Delta(f - f_M)$ becomes Δ independent, as also illustrated in Figure 28, which furthermore shows that the Ξ dependence is logarithmic. More precisely, we have

$$\frac{f - f_M}{f_M} \simeq \frac{\alpha(\log \Xi - \delta)}{\Delta} \quad (42)$$

with α and δ dimensionless parameters reported in Table 2. All previously described effects are encoded within this ultimate expression. Note however that this result cannot hold for arbitrary large $\Xi,$ for f again has to remain smaller than unity. Hence, and similarly to small Δ results, full condensation with $f = 1$ is achieved

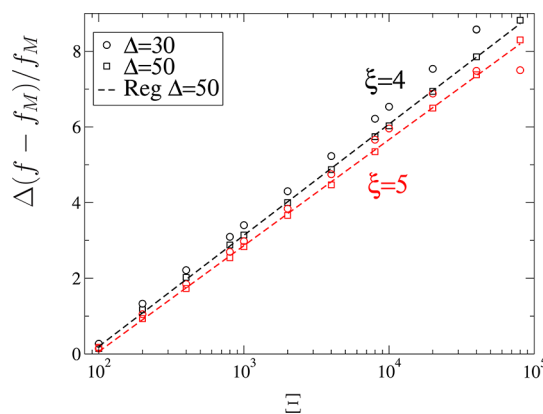


Figure 28. Same as Figure 27, to probe the Ξ dependence in a log–linear plot. The dashed lines represent linear regressions that are summarized in Table 2. Note that, since f is bounded from above by 1 (complete condensation), the quantity plotted cannot grow without bounds which explains the departure from scaling at large $\Xi.$

Table 2. Numerical Values for α and δ from a Regression Performed Considering $(f - f_M)/f_M \simeq \alpha(\log \Xi - \delta)/\Delta$ on Multiple Results^a

Δ	ξ	δ	σ_δ	α	σ_α
30	4	4.42	0.03	1.37	0.01
50	4	4.45	0.02	1.276	0.007
60	4	4.42	0.03	1.228	0.009
300	4	3.9	0.2	1.01	0.05
30	5	4.50	0.04	1.25	0.01
50	5	4.55	0.03	1.22	0.01

^aThe quantities labeled σ refer to the standard deviations.

at large couplings while holding a fixed size (see the $\xi = 5$ and $\Delta = 30$ last two points).

Another interesting feature emerging from Figure 28 and Table 2 is that the x -axis intercept (δ) is the same—within numerical accuracy—for the different sets ($\delta \simeq 4.5$). Consequently, for any given value of the coupling below $e^\delta,$ the system will exhibit “ideal” evaporation (Manning evaporation or $f = f_M$) regardless of the size and, from the data, also regardless of the Manning parameter. This leads us to believe that it is a universal property in the evaporation of ions. Together with the fact that α takes values close to unity except for too small $\Delta,$ we summarize our finite-size analysis with the expression

$$\frac{f - f_M}{f_M} \simeq \frac{(\log \Xi - 4.5)}{\Delta} \quad (43)$$

which holds provided $\Xi > e^\delta \simeq 90$ and $\Delta > \Delta_l,$ while $f \simeq f_M$ for $\Xi < e^\delta.$ Full condensation determines Δ_l (at $f = 1$) in such a way that

$$\Delta_l \simeq (\xi - 1)(\log \Xi - 4.5) \quad (44)$$

It should be kept in mind that $\Delta = \log(D/R)$ measures the log-size of the system.

7. CONCLUSIONS

The behavior of counterions at a planar interface is encoded in the coupling parameter $\Xi,$ defined from the uniform surface charge σ as $\Xi \propto l_b^2 \sigma q^3.$ This scaling simply follows from the fact that the relevant Bjerrum length for q -valent ions is $q^2 l_b,$ and

that the natural measure of surface charge is σ/q . Hence, the dimensionless charge is $(q^2 l_B)^2 \sigma/q$. Equivalently, we can view Ξ (or more precisely $\sqrt{\Xi}$) as the ratio of thermal energy over the typical Coulomb pair repulsion when all ions are condensed onto the plane, and where the interion distance reads $a \propto (q/\sigma)^{1/2}$: $\Xi^{1/2} = (q^2 l_B)/a$. For large Ξ , the ions are confined in a region with extension given by the Gouy length $\mu \propto (l_B \sigma q)^{-1}$. This applies to all coupling regimes, from mean field at small Ξ to strong coupling.¹⁴ When considering curvature, and addressing cylindrical macro-ions rather than planar, a new parameter enters the description, $\xi = q l_B \lambda = q l_B 2\pi R \sigma$. Of course, when $R \gg a$, which also means $\xi \gg \Xi^{1/2}$, the situation is very close to its planar counterpart. It changes significantly in the opposite case $\xi \ll \Xi^{1/2}$ where curvature is strong,¹⁸ and that we called here the needle limit. There, the ions are confined in a region of extension R , given by the radius of the charged rod, that is Ξ -independent. In the needle regime, the radius R is much smaller than the typical distance a' between charges along the rod ($R \ll a \ll a'$). This provides the rationale for deriving simple strong-coupling (SC) predictions: in the sense $R \ll a'$, the ions are far away from each other, and mostly respond to the log potential of the rod. A single particle picture holds, that can be seen as the ideal gas behavior of non-interacting particles in an external field (leaving aside the subtlety of counterion evaporation, that is a collective effect). Good agreement with Monte Carlo results can then be achieved, even at “small” values of ξ . This even if, strictly speaking, the ground state of the system is approached when both Ξ and ξ are large. The reason is that the single particle picture is already an acceptable approximation when ξ is of order unity (or slightly beyond), provided Ξ is large. We also add that, again for large Ξ where the ions remain close to the cylinder, the Manning parameter ξ controls the essentially one-dimensional structure of the ionic system, from a repulsive liquid at small ξ to a crystal at large ξ . Indeed, although ξ is initially defined as the dimensionless linear charge of the rod, it can be rewritten as $q^2 l_B/a'$, and thus qualifies as a one-dimensional plasma parameter, quantifying the strength of interactions for ions along the rod.

An additional feature pertaining to cylindrical charged macromolecules is the counterion condensation–evaporation phenomenon, that plays a prominent role here. While its influence on the mean field behavior is well-known, we have shown that due account of its effect is essential for a good agreement between the SC theory and simulations. We have explicitly worked out the leading ionic profile under large Ξ (SC-0), together with the first correction (SC-1), that indeed improves upon SC-0 but requires quite large values of ξ to be relevant ($\xi > 10$). We also illustrated clearly that the ionic profile, even at large Ξ , crosses over to mean field behavior far from the plate. This behavior, although expected, is in other settings extremely difficult to observe and could only be evidenced due to the (exponentially) large sizes used in the simulations.

We have performed a finite-size analysis for the condensed fraction, which leads to several novel features. To this end, we proposed modifications to the previously introduced Monte Carlo sampling method,⁹ that significantly improved the convergence rate. The signature of finite size effects is logarithmic both in the coupling parameter and in system size, provided Ξ is above $e^{\delta} \sim 90$. Full condensation can be achieved for both small Δ and large Ξ .

Since our work bears some similarities to refs 5 and 9, we have kept the same notations, and we now summarize the main differences. First of all, while our leading SC ionic profiles have the same functional forms, they are not normalized identically. We

have seen that it is indeed important to account for ionic evaporation, as done here. Second, we have worked out the correction to the leading SC expressions, a task that cannot be achieved following the virial route of refs 5 and 9. Third, we have discussed in detail the crossover to mean field at large distances for the ionic densities, evidenced by the simulations. This corroborates the previous studies, where the analysis was not local, but restricted to integrated quantities. Finally, particular attention was paid to finite-size effects that are unusually prevalent in the present system, with particular emphasis on the evaporated fraction.

Before concluding, we provide some parameter values for an important rod-like biopolymer. With double-stranded DNA, one has in water at room temperature $l_B \simeq 7 \text{ \AA}$, $\xi \simeq 8$ and $\Xi \simeq 22$ with divalent ions $q = 2$, and $\xi \simeq 16$ and $\Xi \simeq 180$ with tetravalent ions. This latter case is not quite in the needle limit, since $\xi/\Xi^{1/2}$ is of order 1, but approaching it. The expressions derived here, which are salt-free, would then provide a zeroth order limiting case.

Interesting perspectives opened by this work include dielectric systems, the study of the effect of salt (added electrolyte), together with working out the two-dimensional pendant of our investigation,^{9,42} where ions interact with a log potential, which should lead to a large distance physics that is no longer of mean field type.⁴³

■ ASSOCIATED CONTENT

📄 Supporting Information

The three complementary sections describe the calculation of the interparticle potential and the density profile of counterions, the Ewald summation for the one-dimensional periodic boundary conditions, and some definitions of special functions used throughout the article. This material is available free of charge via the Internet at <http://pubs.acs.org>.

■ AUTHOR INFORMATION

✉ Corresponding Author

*Phone: +57 1 3394949 Ext. 5165 (J.P.M.); +57 1 3394949 Ext. 2749 (G.T.); +33 1 69 15 73 39 (E.T.).

Notes

The authors declare no competing financial interest.

■ ACKNOWLEDGMENTS

We would like to thank Ladislav Šamaj for stimulating discussions and Martial Mazars for insightful advice on the simulation code. Support from ECOS Nord/COLCIENCIAS-MEN-ICETEX is acknowledged. J.P.M. and G.T. acknowledge partial financial support from Comité de Investigaciones, Facultad de Ciencias, Universidad de los Andes.

■ REFERENCES

- (1) (a) Manning, G. Limiting Laws and Counterion Condensation in Polyelectrolyte Solutions I. Colligative Properties. *J. Chem. Phys.* **1969**, *51*, 924. (b) Manning, G. Limiting Laws and Counterion Condensation in Polyelectrolyte Solutions II. Self-Diffusion of the Small Ions. *J. Chem. Phys.* **1969**, *51*, 934. (c) Manning, G. Limiting Laws and Counterion Condensation in Polyelectrolyte Solutions. III. An Analysis Based on the Mayer Ionic Solution Theory. *J. Chem. Phys.* **1969**, *51*, 3249.
- (2) Oosawa, F. *Polyelectrolytes*; Marcel Dekker: New York, 1971.
- (3) Ramanathan, G. V. Statistical Mechanics of Electrolytes and Polyelectrolytes. III. The Cylindrical Poisson–Boltzmann Equation. *J. Chem. Phys.* **1983**, *78*, 3223–3232.
- (4) (a) Rouzina, I.; Bloomfield, V. A. Competitive Electrostatic Binding of Charged Ligands to Polyelectrolytes: Practical Approach Using the Nonlinear Poisson–Boltzmann Equation. *Biophys. Chem.*

- 1997, 64, 139–155. (b) Levin, Y.; Barbosa, M. C. Thermodynamic Theory of Counterion Association in Rigid Polyelectrolytes. *J. Phys. II* 1997, 7, 37–55. (c) Deshkovski, A.; Obukhov, S.; Rubinstein, M. Counterion Phase Transitions in Dilute Polyelectrolyte Solutions. *Phys. Rev. Lett.* 2001, 86, 2341–2344. (d) Hansen, P. L.; Podgornik, R.; Parsegian, V. A. Osmotic Properties of DNA: Critical Evaluation of Counterion Condensation Theory. *Phys. Rev. E* 2001, 64, 021907. (e) Deserno, M.; Holm, C.; Blaul, J.; Ballauff, M.; Rehahn, M. The Osmotic Coefficient of Rod-Like Polyelectrolytes: Computer Simulation, Analytical Theory, and Experiment. *Eur. Phys. J. E* 2001, 5, 97–103. (f) Henle, M. L.; Santangelo, C. D.; Patel, D. M.; Pincus, P. A. Distribution of Counterions near Discretely Charged Planes and Rods. *Europhys. Lett.* 2004, 66, 284. (g) Muthukumar, M. Theory of Counter-ion Condensation on Flexible Polyelectrolytes: Adsorption Mechanism. *J. Chem. Phys.* 2004, 120, 9343–9350.
- (5) Naji, A.; Netz, R. R. Counterions at Charged Cylinders: Criticality and Universality beyond Mean-Field Theory. *Phys. Rev. Lett.* 2005, 95, 185703.
- (6) Trizac, E.; Téllez, G. Onsager-Manning-Oosawa Condensation Phenomenon and the Effect of Salt. *Phys. Rev. Lett.* 2006, 96, 38302.
- (7) Levin, Y. Electrostatic Correlations: from Plasma to Biology. *Rep. Prog. Phys.* 2002, 65, 1577.
- (8) Grosberg, A. Y.; Nguyen, T. T.; Shklovskii, B. I. *Colloquium: The Physics of Charge Inversion in Chemical and Biological Systems. Rev. Mod. Phys.* 2002, 74, 329–345.
- (9) Naji, A.; Netz, R. R. Scaling and Universality in the Counterion-Condensation Transition at Charged Cylinders. *Phys. Rev. E* 2006, 73, 056105.
- (10) Boroudjerdi, H.; Kim, Y.-W.; Naji, A.; Netz, R.; Schlagberger, X.; Serr, A. Statics and Dynamics of Strongly Charged Soft Matter. *Phys. Rep.* 2005, 416, 129–199.
- (11) Messina, R. Electrostatics in Soft Matter. *J. Phys.: Condens. Matter* 2009, 21, 113102.
- (12) Andelman, D. *Soft Condensed Matter Physics in Molecular and Cell Biology*; Scottish Graduate Series; Taylor & Francis: New York, 2006; Chapter 6, pp 97–122.
- (13) Šamaj, L.; Trizac, E. Counterions at Highly Charged Interfaces: From One Plate to Like-Charge Attraction. *Phys. Rev. Lett.* 2011, 106, 078301.
- (14) Netz, R. Electrostatics of Counter-ions at and between Planar Charged Walls: From Poisson-Boltzmann to the Strong-Coupling Theory. *Eur. Phys. J. E: Soft Matter Biol. Phys.* 2001, 5, 557–574.
- (15) Kanduč, M.; Trulsson, M.; Naji, A.; Burak, Y.; Forsman, J.; Podgornik, R. Weak and Strong-Coupling Electrostatic Interactions between Asymmetrically Charged Planar Surfaces. *Phys. Rev. E* 2008, 78, 061105.
- (16) Šamaj, L.; Trizac, E. Wigner-Crystal Formulation of Strong-Coupling Theory for Counterions near Planar Charged Interfaces. *Phys. Rev. E* 2011, 84, 041401.
- (17) It is customary to introduce the Gouy length $\mu = (2\pi l_B \sigma q)^{-1}$. We then have $\Xi = l_B q^2 / \mu$,²⁰ and likewise $\xi = R / \mu$.⁵ Since the interesting regime is for $\xi > 1$, μ is always the smallest length scale in the problem. In the needle limit, where $\Xi^{1/2} \gg \xi$, we have in general $\mu < R \ll a \ll a'$. The relation between a' and $q^2 l_B$ is given by ξ , with roughly $q^2 l_B = a' \simeq \xi$ (taking due account of counterion condensation, which affects a' , we get $q^2 l_B = a' = \xi - 1$).
- (18) Arnold, A.; Holm, C. Interactions of Like-Charged Rods at Low Temperatures: Analytical Theory vs. Simulations. *Eur. Phys. J. E* 2008, 27, 21.
- (19) Kanduč, M.; Naji, A.; Podgornik, R. Counterion-mediated Weak and Strong Coupling Electrostatic Interaction between Like-Charged Cylindrical Dielectrics. *J. Chem. Phys.* 2010, 132, 224703.
- (20) Moreira, A.; Netz, R. Strong-Coupling Theory for Counter-Ion Distributions. *Europhys. Lett.* 2000, 52, 705.
- (21) Moreira, A.; Netz, R. Binding of Similarly Charged Plates with Counterions Only. *Phys. Rev. Lett.* 2001, 87, 78301.
- (22) Katchalsky, A. Polyelectrolytes. *Pure Appl. Chem.* 1971, 26, 327–374.
- (23) Fuoss, R.; Katchalsky, A.; Lifson, S. The Potential of an Infinite Rod-Like Molecule and the Distribution of the Counter Ions. *Proc. Natl. Acad. Sci. U.S.A.* 1951, 37, 579.
- (24) Lifson, S.; Katchalsky, A. The Electrostatic Free Energy of Polyelectrolyte Solutions. II. Fully Stretched Macromolecules. *J. Polym. Sci.* 1954, 13, 43–55.
- (25) Liouville, J. Sur l'Équation aux Différences Partielles ($\partial^2 \log \lambda / \partial u \partial v$) $\pm (\lambda / 2a^2) = 0$. *J. Math. Pures Appl.* 1853, 71–72.
- (26) Henderson, D.; Blum, L.; Lebowitz, J. L. An Exact Formula for the Contact Value of the Density Profile of a System of Charged Hard Spheres near a Charged Wall. *J. Electroanal. Chem. Interfacial Electrochem.* 1979, 102, 315–319.
- (27) Deserno, M.; Holm, C.; May, S. Fraction of Condensed Counterions around a Charged Rod: Comparison of Poisson-Boltzmann Theory and Computer Simulations. *Macromolecules* 2000, 33, 199–206.
- (28) Qian, H.; Schellman, J. Transformed Poisson-Boltzmann Relations and Ionic Distributions. *J. Phys. Chem. B* 2000, 104, 11528–11540.
- (29) Téllez, G.; Trizac, E. Exact Asymptotic Expansions for the Cylindrical Poisson-Boltzmann Equation. *J. Stat. Mech.: Theory Exp.* 2006, 2006, P06018.
- (30) Mazars, M. Lekner Summations. *J. Chem. Phys.* 2001, 115, 2955.
- (31) Mazars, M. Lekner Summations and Ewald Summations for Quasi-Two-Dimensional Systems. *Mol. Phys.* 2005, 103, 1241–1260.
- (32) Deserno, M.; Holm, C. How to Mesh up Ewald Sums. I. A Theoretical and Numerical Comparison of Various Particle Mesh Routines. *J. Chem. Phys.* 1998, 109, 7678.
- (33) Arnold, A.; Holm, C. MMM1D: A Method for Calculating Electrostatic Interactions in One-Dimensional Periodic Geometries. *J. Chem. Phys.* 2005, 123, 144103.
- (34) Limbach, H.; Arnold, A.; Mann, B.; Holm, C. ESPResSo—an Extensible Simulation Package for Research on Soft Matter Systems. *Comput. Phys. Commun.* 2006, 174, 704–727.
- (35) Mazars, M. Ewald Methods for Inverse Power-Law Interactions in Tridimensional and Quasi-Two-Dimensional Systems. *J. Phys. A: Math. Theor.* 2010, 43, 425002.
- (36) Harris, F. Incomplete Bessel, Generalized Incomplete Gamma, or Leaky Aquifer Functions. *J. Comput. Appl. Math.* 2008, 215, 260–269.
- (37) Harris, F. E.; Fripiat, J. G. Methods for Incomplete Bessel Function Evaluation. *Int. J. Quantum Chem.* 2009, 109, 1728–1740.
- (38) Shklovskii, B. Screening of a Macroion by Multivalents: Correlation-Induced Inversion of Charge. *Phys. Rev. E* 1999, 60, 5802–5811.
- (39) Chen, Y.-G.; Weeks, J. D. Local Molecular Field Theory for Effective Attractions between Like Charged Objects in Systems with Strong Coulomb Interactions. *Proc. Natl. Acad. Sci. U.S.A.* 2006, 103, 7560–7565.
- (40) dos Santos, A. P.; Diehl, A.; Levin, Y. Electrostatic Correlations in Colloidal Suspensions: Density Profiles and Effective Charges beyond the Poisson-Boltzmann Theory. *J. Chem. Phys.* 2009, 130, 124110.
- (41) Moreira, A.; Netz, R. Simulations of Counterions at Charged Plates. *Eur. Phys. J. E* 2002, 8, 33–58.
- (42) Burak, Y.; Orland, H. Manning Condensation in Two Dimensions. *Phys. Rev. E* 2006, 73, 010501.
- (43) Šamaj, L.; Trizac, E. Counter-ions at Charged Walls: Two-Dimensional Systems. *Eur. Phys. J. E* 2011, 34, 20.